# Probing Magnetic Defects in Ultra-Scaled Nanowires with Optically Detected Spin Resonance in Nitrogen-Vacancy Center in Diamond

Umberto Celano,* Hai Zhong, Florin Ciubotaru, Laurentiu Stoleriu, Alexander Stark, Peter Rickhaus, Felipe Fávaro de Oliveira, Mathieu Munsch, Paola Favia, Maxim Korytov, Patricia Van Marcke, Patrick Maletinsky, Christoph Adelmann, and Paul van der Heide

Read Online

ACCESS | Metrics & More | Article Recommendations | Supporting Information

**ABSTRACT:** Magnetic nanowires (NWs) are essential building blocks of spintronics devices as they offer tunable magnetic properties and anisotropy through their geometry. While the synthesis and compositional control of NWs have seen major improvements, considerable challenges remain for the characterization of local magnetic features at the nanoscale. Here, we demonstrate nonperturbative field distribution mapping in ultra-scaled magnetic nanowires with diameters down to 6 nm by scanning nitrogen-vacancy magnetometry. This enables localized, minimally invasive magnetic imaging with sensitivity down to 3 $\mu$T Hz$^{-1/2}$. The imaging reveals the presence of weak magnetic inhomogeneities inside in-plane magnetized nanowires that are largely undetectable with standard metrology and can be related to local fluctuations of the NWs' saturation magnetization. In addition, the strong magnetic field confinement in the nanowires allows for the study of the interaction between the stray magnetic field and the nitrogen-vacancy sensor, thus clarifying the contrasting formation mechanisms for technologically relevant magnetic nanostructures.

**KEYWORDS:** *magnetic nanowires, Nitrogen-vacancy, scanning Nitrogen-vacancy magnetometry, SNVM*
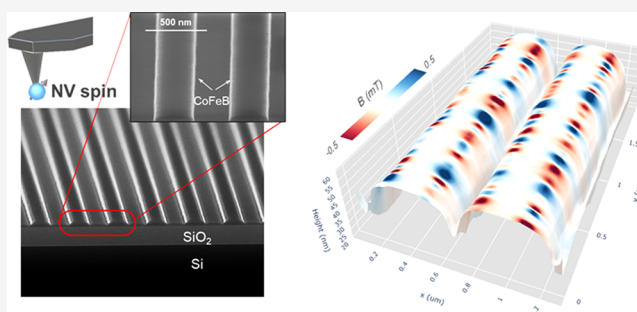
## INTRODUCTION

Patterned magnetic nanowires (NWs) are an ideal medium for fast propagation of domain walls (DWs) or spin waves in the ever-growing field of spintronic devices.[1−3] Most importantly, NWs are a convenient architecture to obtain bistable magnetic configurations with a single magnetic easy axis and with anisotropic magnetic properties that can be adjusted by the wire geometry. For high density data storage and computation, scaled nanowires architectures (with wire widths of the order of 10 to 100 nm) are generally considered as frontrunners for emerging device concepts.[2,4−9] As an example, much research has been devoted to the engineering and control of the dynamic switching behavior of nanomagnets and magnetic NWs for memory and logic applications by manipulating the movement and positioning of DWs. Advanced characterization methods, such as magnetic force microscopy (MFM) or X-ray photoemission electron microscopy (XPEEM), have been instrumental for these studies, offering magnetic sensitivity in the sub-20 nm spatial resolution for ferromagnetic domains and additional information on the local chemistry, including oxidation states and coordination numbers for X-ray techniques.[10−13] Despite much encouraging progress in manufacturing technology, scaled NWs still host a wide range of stochastic magnetic nonuniformities and defects,

which present major challenges for the control of their properties.[3,14] Here, due to the small scales involved and the potentially weak magnitudes of these defects, their physical characterization is very demanding and thus their properties and impact are not yet well understood. In this work, it has become increasingly clear that even weak magnetic defects and localized inhomogeneities can have a major impact on the magnetic switching of NWs-based devices by acting as DW pinning sites. While these results have opened pathways toward new devices based on DW manipulation, the localized sensing of individual defects, the nonperturbing characterization of weak magnetic field distribution over large areas, and the reconstruction of the three-dimensional field orientation remain highly challenging while being clearly central in the development of future NW-based spintronic devices. In such devices, nanoscale defects such as internanowire gaps,
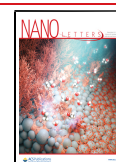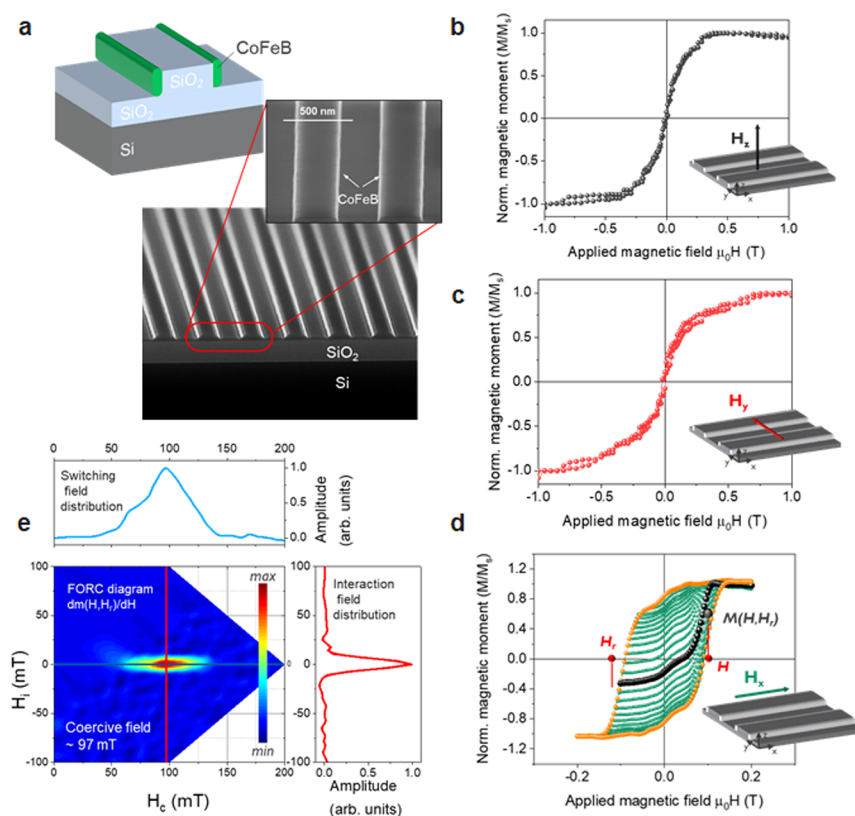
**Figure 1.** Sample description and nanowire magnetization. (a) Schematic of the sample under study and top view SEM images of the nanowires. (b−d) Magnetization loops M(H) measured by vibrating sample magnetometry for different orientations of the external applied magnetic field with respect the magnetic NW geometry, as indicated in the insets. (d) First-order reversal curves measured by applying the external magnetic field along the wires. (e) Coercive and interaction field distributions determined from the FORC measurements. Extracted profiles show the switching field (blue) and interaction field distributions (red).

fluctuations in the saturation magnetization, or grain boundaries perpendicular to the NW direction can introduce weak magnetic perturbations, which are often too small to be detected by conventional methods. Alternatively, similar effects can be induced by various types of DWs in in-plane magnetized NWs, including vortex and transverse DWs, that are characterized by different types of magnetization rotation parallel to the NW. Thus, characterization methods can directly probe such nanoscopic weak magnetic defects can have great impact on the ability to control and to tailor the spin and DW transport in many emerging spintronic devices.

Here, by leveraging state-of-the-art fabrication and sensing methods, we demonstrate nonperturbative probing of individual magnetic inhomogeneities which are contained in in-plane magnetized nanowire arrays. This is obtained by using a scanning nitrogen-vacancy magnetometer (SNVM) resolving individual inhomogeneities in wires with a width of 6 nm, over hundreds of micrometer square regions, in ambient conditions and at noncryogenic temperatures. In SNVM, nitrogen-vacancy centers in diamond are used as atomic-size sensors to implement magnetometry based on an atomic force microscopy scheme.[15] NV centers in diamond have recently attracted the attention of the community hosting a coherent, single electron spin used in quantum sensing, and magnetometry.[15] The stable fluorescence of NV centers can be used for the optical detection of magnetic resonance of the electron spin, thus enabling an optimal coupling between light emission and magnetic field. As a consequence, one can obtain real-space quantitative magnetic-field images in ambient conditions

with unprecedented spatial resolution and sensitivity.[16] Given the rather complex nature of the contrast in scanning nitrogen-vacancy magnetometer, we discuss the origin of contrast in such inhomogeneities supported by micromagnetic simulations and the use of transmission electron microscopy (TEM) images. We observe excellent correlations between experimental results and simulations for the studied NW geometry and demonstrate a lateral resolution of SNVM of about 50 nm. This work paves the way for an optimized methodology based on optically detected electron spin resonance (ESR) in SNVM that allows for the quantitative sensing of ultraweak magnetic defects in $\mu$T range in technologically relevant device structures.

## ■ MAIN

The studied sample consists of an array of CoFeB NWs with cross-sectional areas of about 120 $nm^2$, a wire width of about 6 nm, and mm lengths. The NWs are fabricated by a self-aligned subtractive patterning scheme (Supporting Information Figure S1).[17] In this scheme, a CoFeB film is deposited over a prepatterned $SiO_2$ cores with widths of 300 nm and pitches of 600 nm. The CoFeB films are then anisotropically etched using ion-beam etching on flat regions on top of and between $SiO_2$ cores, leaving only CoFeB at the sidewalls. This allows NWs to be patterned over large areas using standard lithographic techniques with much lower resolution. Note that the NW width is determined by the initial CoFeB film thickness rather than by the resolution of the lithograph process (Figure 1a). Using this method, NWs with widths down to 3 nm have been
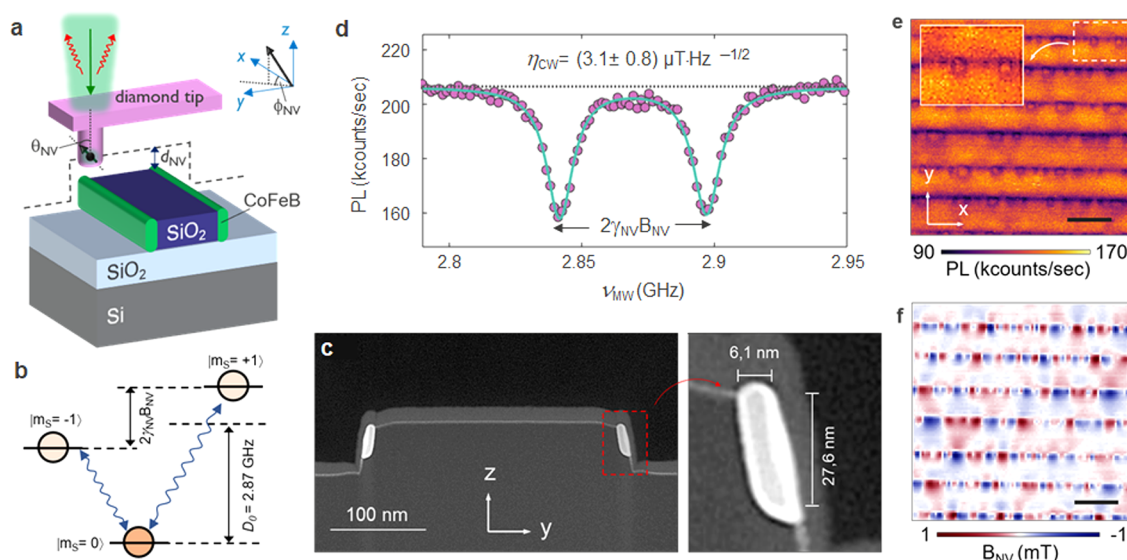
**Figure 2.** Imaging CoFeB nanostructures using SNVM. (a) Schematic of the SNVM experimental setup with optically detected electron spin resonance of the single scanning NV center. The NV center is stabilized at a fixed scanning height following the surface topographical profiles using atomic force feedback, ensuring that the tip-to-sample distance is the same throughout the whole image. (b) NV center ground state spin levels with zero-field splitting $D_0$ and Zeeman splitting $2\gamma_{NV}B_{NV}$ (with $\gamma_{NV}$ = 28 GHz/T and $B_{NV}$ the local magnetic field projected along the NV quantization axis). As indicated by the schematic, the $|m_s = 0\rangle$ spin sublevel exhibits a higher fluorescence rate than $|m_s = \pm 1\rangle$. (c) Cross-section scanning transmission electron microscopy image of the sample obtained in a high-angle annular dark field imaging (STEM-HAADF) mode. The thin profile over the surface contours indicates the presence of ca. 1 nm oxidized shell surrounding the wire core. (d) The component of the stray field along the NV quantization axis is measured as a PL count. (e) Photoluminescence quenching image recorded with SNVM above the sample surface, showing an overview of contrast generated only in the location of the NWs. Static magnetic field distribution is acquired over the same location.

fabricated at pitches in the 150 nm range, and with large area $(mm^2)$ coverage.[17] Scanning electron microscopy and TEM images of the nanowire structural details are shown in Supporting Information Figure S2. Both high resolution and dark-field TEM show that CoFeB is amorphous. The CoFeB NWs exhibit a strong magnetic anisotropy with the easy axis being in-plane along the wire. This is demonstrated by the hysteresis loops in Figure 1b−d along different directions that were measured by vibrating sample magnetometry. Since the magnetic volume of a single wire is too small to be detected by this technique, the magnetization loops were measured on a macroscopic $(mm^2)$ sample that includes about 16 000 parallel NWs, uniformly distributed over the area. Figure 1b and 1c indicate no remanent magnetization for transversal magnetic bias fields (both in-plane and out-of-plane), whereas Figure 1d demonstrates a clear hysteresis loop with a coercive field around 100 mT for longitudinal fields. Note that the loop in Figure 1d is not square as expected for ideal nanowires due to shape anisotropy. This can be related to nonuniformities within individual NW or, more probably, to variations between NWs that can be related to both (or either) their magnetic and physical structures. To further analyze the variability within the ensemble of NWs, first-order reversal curve (FORC) measurements (Figure 1d) have been performed. The FORC method[18] is a statistical approach to study the distribution of switching processes in an ensemble of magnetic structures. A FORC is obtained by saturating the magnetization of the sample, applying a reversal field up to a certain value $H_r$, and finally measuring M(H) again for increasing magnetic field until saturation is reached again. Different values of $H_r$ allow for the construction of a set of FORC graphs that cover the entire hysteresis loop (Figure 1d). The data can then be analyzed by applying a mixed second-order derivative of $M(H_r,H)$, from

which the distributions of coercive and interaction magnetic fields in the NW ensemble can be extracted (Figure 1e; see also Supporting Information Figure S3). The FORC diagram in Figure 1e demonstrates rather narrow distributions of both switching and interaction fields, indicating that the NWs all possess similar properties. The narrow coercive field distribution centered around 100 mT suggest that the NWs are magnetically uniform (with similar individual switching fields) whereas the tight interaction field distribution centered around zero indicates weak magnetic interactions between the NWs. Thus, the FORC analysis allows for a statistical analysis of the magnetic properties of the NW ensemble. However, the nature of small nonuniformities in individual NWs that give rise to the distribution cannot be assessed by this method. As demonstrated below, this can be achieved by SNVM.

In the next step, we demonstrate nonperturbative field distribution mapping of the structures in Figure 1a. The magnetic imaging is performed with a commercial SNVM (ProteusQ, Qnami AG) operating under ambient conditions. A diamond tip hosting a single NV defect at its apex (Qnami, Quantilever MX) was integrated on a quartz tuning fork-based frequency modulation atomic force microscope (FM-AFM) and scanned above the CoFeB NW structure (see Figure 2a for a schematic of the experiment). The ground state of negatively charged NV center is a spin triplet, consisting of the magnetic sublevels $|m_s = 0\rangle$ and $|m_s = \pm1\rangle$ as shown in Figure 2b, where $m_s$ refers to the magnetic quantum number along the NV quantization axis.[15] With the absence of external magnetic field, the states $|m_s = \pm 1\rangle$ are degenerate and a split by $D_0 = 2.87$ GHz from $|m_s = 0\rangle$. When an external magnetic field along the NV axis is applied, it induces a Zeeman splitting $2\gamma_{NV}B_{NV}$ of the sublevels $|m_s = \pm 1\rangle$, where $\gamma_{NV}$ = 28 GHz/T is the gyromagnetic ratio (cf. Figure 2b) and $B_{NV}$ is the detected
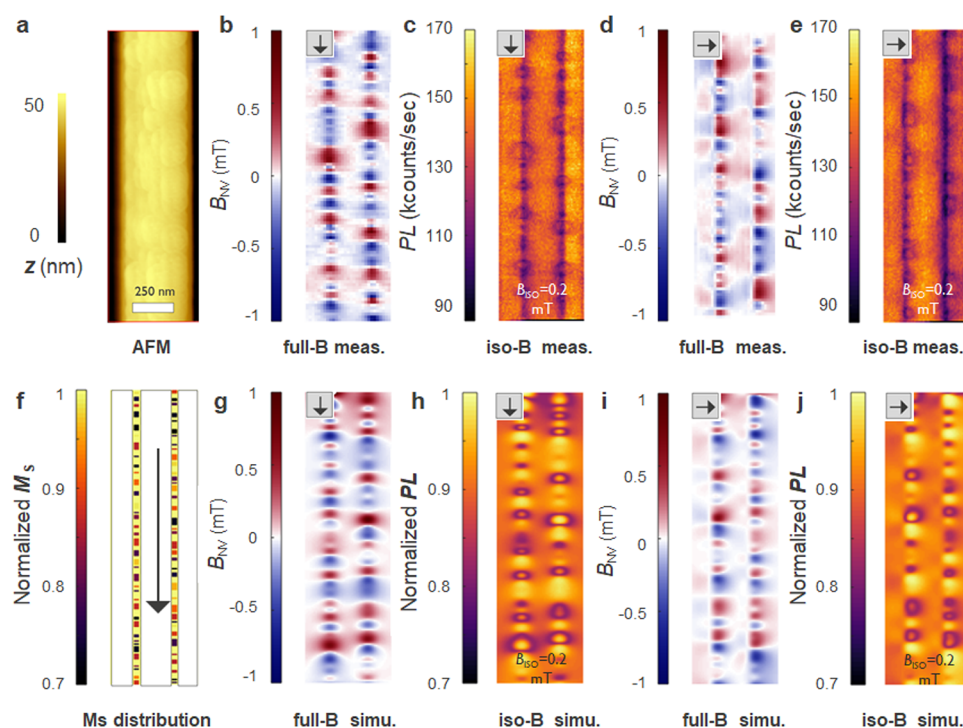
**Figure 3.** AFM/SNVM experiments and SNVM simulation. (a) AFM image of a nanostripe structure with two CoFeB NWs on both of its sides. (b and d) Full B images of the two NWs recorded at different locations and at different relative NV-tip orientations. (c and e) Corresponding iso-magnetic images of the same scan area for the magnetic field component $B_{NV} = 0.2$ mT. (f) randomly generated $M_s$ pattern along the NWs with $M_s$ in the range of 0.7–1 $M_{s,max}$ ($M_{s,max} = 1200$ emu/cm$^3$). The simulated SNVM images based on the $M_s$ pattern with $d_{NV} = 50$ nm are shown in (g) and (i) (full B images), as well as in (h) and (j) (iso-magnetic images) for different relative NV-tip orientations, respectively. The NV projection axis in the imaging plan is indicated by the arrow shown in (b−e) and (g−j). All images have the same size with the scale bar shown in (a).

magnetic field projected on the NV quantization axis. The NV spin is initialized with 515 nm green laser, and its red photoluminescence (PL) signal is optically read out via the confocal microscope module in our setup. These combined properties enable optical detection of electron spin resonance (ESR) of NV centers after initialization into the fluorescent bright $|m_s = 0\rangle$ state. A near-field microwave wire (placed ~20 $\mu$m apart from the NV tip in the microscope) generates a driving field resonant with either of the $|m_s = 0\rangle$ to $|m_s = \pm 1\rangle$ transitions that populate the less fluorescent $|m_s = \pm 1\rangle$ states, resulting in a significant drop in NV fluorescence (Figure 2c), here with an ESR contrast of ~24%. The frequency difference of the two resonance dips thus yields a direct quantitative measure of $B_{NV}$ in a self-calibrated manner, via the simple relation of $D\upsilon = 2\gamma_{NV}B_{NV}$. By fitting the ESR spectrum,[16] a continuous wave (CW) dc magnetic sensitivity of ~3 $\mu$T/$\sqrt{Hz}$ has been confirmed (Figure 2d). In the following, all experiments are performed under ambient conditions with a bias field $B_b \approx 1$ mT applied along the NV defect axis to determine the sign of the measured magnetic fields.[15] During the scans, the frequency shift of the quartz tuning fork mechanical oscillator, to which the diamond tip is attached ($\Delta f = 5$ Hz for all the measurements in this paper), is used as the z-feedback, to ensure a constant the tip−sample distance $d_{NV}$. This distance is calibrated to be $d_{NV} = 59.7 \pm 1.8$ nm through a calibration process above the edges of a uniformly magnetized ferromagnetic strip (Supporting Information Figure S4). The NV center orientation is characterized by the polar angle $\theta = 57.1° \pm 2.5°$ and the azimuthal angle $\phi = 270.3° \pm 0.9°$, respectively in the laboratory coordinator defined in Figure 2a

(for details of the calibration, cf. Supporting Information Figure S4).

To determine the full magnetic field $B_{NV}$ distribution, an ESR spectrum is recorded at each pixel during the scan ("full-B" mode). The pixel integration time of 4.5 s is used in all the full-B mode images to ensure a reasonable signal-to-noise ratio. This, however, translates in relatively long imaging times, i.e., ~25 min for the iso-B mode (200 × 200 pixel) and about 13.5 h for full-B mode (100 × 100 pixels) (see Figure 2f). Still, a preliminary fast characterization of a magnetic field distribution is also possible by imaging iso-magnetic field contours ("iso-B" mode for short) with a pixel dwell time of only 20 ms (cf. Figures 2e). In the iso-B mode imaging mode, as described in detail by Rondin et al.,[15] the NV defect PL intensity is monitored while scanning the magnetic sample and simultaneously applying a continuous wave microwave—signal with a predefined frequency $\nu_{iso}$. The PL image then exhibits dark contours of reduced PL intensity whenever the electron spin transition is in resonance with the chosen microwave frequency at each scanned pixel site. Thus, any iso-B contour can be imaged by preselecting the appropriate microwave frequency. Although very fast as a preliminary overview characterization, this method is sensitive to the background luminescence from the sample since any luminescence evolution not linked to the NV defect adds a bias on the iso-magnetic field images. In the iso-B mode, however, only one magnetic field component (i.e., local magnetic field projected along the NV quantization axis; cf. Figure 2a) across the scanned area is probed. For all the full-B mode images, the stray magnetic field in the range of ±1 mT is revealed along all the CoFeB NWs. Clearly, the combination of high NW density and low magnetic stray field strength
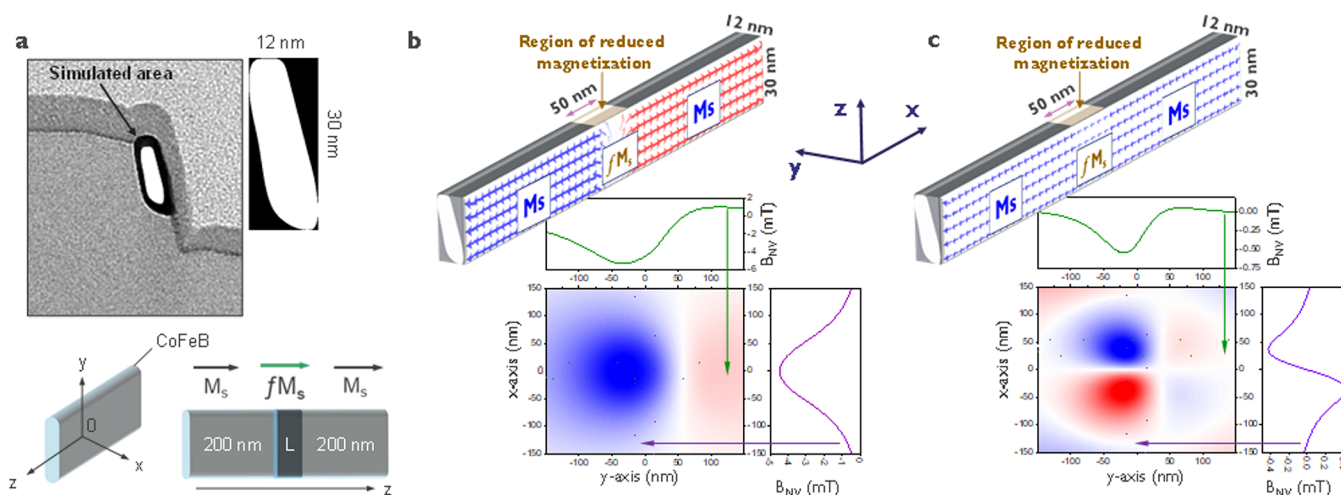
**Figure 4.** Micromagnetic simulations. (a) Simulated area and NW dimensions deduced from cross-section TEM images. (b) Magnetization distribution (top) in a CoFeB NW and spatial distribution of the magnetic field projected onto the NV axis for a NW with a domain wall of reduced magnetization ($f = 0.8$), or without a domain wall (c). The magnetic field was extracted at a height of 50 nm above the magnetic nanowire (centered at the $[x = 0, y = 0]$ coordinates), as in the SNVM experiment. The top and left panels correspond to horizontal and vertical cuts of the field distributions, averaged over a 30 nm wide, as indicated by the dashed lines, to match the resolution of the NV detector.

increases the complexity of decoupling the contribution of DWs with the NWs morphology (roughness, disruptions, edges, shape deformations, etc.) and the defectivity (local crystallinity changes, or point defects, etc.). Interestingly, high-resolution TEM and magnetic force microscopy (not shown) do not detect structural or magnetic defects in the NWs with a density comparable to the one observed by SNVM. This indicates that weak magnetic defects can largely go undetected by these techniques, either because they originate from minimal structural/compositional variations in the NW or because they generate weak magnetic perturbations below the probing sensitivity. It is important to note that we repeat the SNVM measurements using different single-NV tips with different NV orientations, as well as rotating the NW orientation with respect to the NV tip; all led to consistent results. In the iso-B PL image shown in Figure 2e, we observe dark lines along the full length of each NW—these dark lines do not correspond to magnetic signal but result from a plasmonic quenching effect as explained elsewhere.[19] However, on top of the dark lines, additional ring-like features are visible (e.g., Figure 2e). The features are positioned either at the side or directly at the center of the NWs at two different orientations of the sample. These features thus depend on the NV orientation with respect to the NW spatial orientation. This is further discussed in the Supporting Information (Figure S5, full-B/iso-B SNVM image simulation).

## NUMERICAL MICROMAGNETIC SIMULATIONS

To interpret the above observations, we have performed SNVM image simulations based on a magnetostatic model that assumes randomly distributed sectors with reduced $M_s$ (up to 30% reduction) along the CoFeB NWs (50 nm, according to TEM results, Supporting Information Figure S6). In the full-B image simulation, using the magnetic vector field at a scan height of $d_{NV}$, the projection along the NV quantization axis $B_{NV}$ can be calculated based on the angular information on the NV defect ($\theta_{NV}$, $\phi_{NV}$) via a scalar product. For iso-B image simulation, one can deduce the PL contrast simply by extracting $B_{NV}$ from the Lorentzian line shape of the ESR spectra as a transfer function. Details about the simulation

process can be found in the Supporting Information. Without loss of generality, we have calculated SNVM images of both NWs near the left and right edges in one nanostripe structure (model shown in Supporting Information Figure S5). Figure 3b and 3c show the full-B and iso-B images of the same area for one sample orientation (in-plane projection of NV axis parallel to the NWs), respectively. In addition, SNVM images with the sample rotated by 90° are shown in Figure 3d and 3e (Note the different scan area compared to Figures 3b and 3c). The $M_s$ distribution along a pair of NWs assumed in the simulations is shown in Figure 3f with a maximal $M_s$ reduction of 30%. Using the simulation procedure (Supporting Information Figures S4 and S5) and a value of $d_{NV}$ of 50 nm, we have simulated SNVM images for the same configurations as used in the experiments (Figure 3g to 3j). The simulated images compare favorably to the experimental ones and show very similar defect shapes and positions. Moreover, the simulated stray field range in Figure 3g and 3i is comparable to the experimental results, i.e., to Figure 3b and 3e. Therefore, we infer that the observed defects can be attributed to small local $M_s$ variations, which may stem from fluctuations in the CoFeB density and stoichiometry or from variations in magnetic anisotropy.

Furthermore, we performed micromagnetic simulations[20] of a single magnetic nanowire with the same cross-section as observed by TEM imaging, considering similar types of nonuniformities as discussed above. Figure 4a shows the simulated area assumed from cross-section TEM. Figure 4b and 4c display the magnetization configurations with and without the presence of a Néel magnetic DW inside a wire. A nonuniformity of 20% reduction of the saturation magnetization over a 50 nm length has been assumed in this case. The projection of the magnetic field created by these magnetic configurations on the NV axis extracted in a plane 50 nm above the wire (as in the experiments) is also presented in Figure 4. The micromagnetic simulations show that the Néel DW (of ca. 40 nm width for the considered case) generates magnetic fields of the order of several mT, which are about 15−20× larger than the experimental findings. By contrast, if no DW exists in the wire and the magnetization is uniform

along the wire as shown in Figure 4b, the generated magnetic fields are of the same magnitude as the fields detected in the SNVM experiments. In addition, the spatial distribution of the fields obtained from simulation matches very well the experimental data (see e.g., Figure 3e). The simulations performed for wires with nonuniformities of different sizes and different saturation magnetization have shown that the generated fields by DWs are always orders of magnitude higher than those observed experimentally. From the simulations, it was further found that the asymmetry in the field distribution with respect to the wire axis originates from the projection of the field on orientation of the NV axis, whereas the field projection on Cartesian coordinates is symmetric (see Supporting Information Figure S6). The micromagnetic simulations also demonstrate very large fields at the ends or at gaps in the wires, which suggests the absence of narrow gaps and grain boundaries perpendicular to the nanowire axis direction that otherwise would introduce magnetic perturbations that should well be detectable by NV-magnetometry. This observation together with a TEM image along the wires support the hypothesis that the wires are physically continuous in the studied area. However, we acknowledge that residual strain introduced during the NWs deposition and/or small geometrical imperfections (as visible in the TEM Figure S2) could also contribute to the contrast detected by the SNVM. Future work could address this uncertainty by comparing NWs grown on straight spacers or curved structures and correlating the results with micromagnetic simulations.

## CONCLUSION

In summary, we have demonstrated a novel ultrasensitive technique to characterize ultrascaled magnetic NWs using SNVM. The results indicate that SNVM can be used as a quantitative method to study nanoscale magnetization variations in individual in-plane magnetized NWs. For the CoFeB nanowires, a high density of weak magnetic inhomogeneities was observed. These magnetic defects could then be studied with high spatial resolution and without magnetic disturbance using both iso-B and full-B modes, which allowed us to obtain quantitative information about the associated magnetic field distribution. The experimental results were validated by micromagnetic simulations of the SNVM contrast using a magnetostatic model. By comparing experimental data with simulations, the observed magnetic defects could be attributed to local inhomogeneities in the NWs (i.e., density, compositional, or strain-induced) that led to fluctuations of the in-plane saturation magnetization. More quantitatively, SNVM allowed detection of local variations $M_s$ in the CoFeB NWs on the order of 30% or less with nanoscale spatial resolution and $\mu$T magnetic field sensitivity. We note that these weak magnetic defects can go largely undetected when conventional characterization approaches are used. Finally, the excellent agreement between experimental and simulated SNVM images demonstrates the capability of the method to sense quantitative weak variations of magnetic properties in ultrascaled magnetic devices. The results also provide insight into the contrasting generation mechanisms, which are critical for the interpretation of SNVM images of spatially confined magnetic structures. Beyond the present work, our results show a clear pathway for the quantitative analysis of novel magnetic materials for spintronic devices at aggressively scaled dimensions.

## ASSOCIATED CONTENT

### Supporting Information

The Supporting Information is available free of charge at https://pubs.acs.org/doi/10.1021/acs.nanolett.1c03723.

We present the details for the fabrication of the in-plane magnetized NWs array and report other details of the structure under study using TEM and SEM. Later, the FORC method and related data analysis is further described including details on the simulations and calibration procedure used for the analysis of full-B/iso-B SNVM image reconstruction. Finally, details on the structures used and quantitative results of the micromagnetic simulations are also shown. (PDF)

## AUTHOR INFORMATION

### Corresponding Author

**Umberto Celano** − imec, 3001 Leuven, Belgium; Faculty of Science and Technology and MESA+ Institute for Nanotechnology, University of Twente, 7500 Enschede, The Netherlands; ◉ orcid.org/0000-0002-2856-3847; Email: umberto.celano@imec.be

### Authors

**Hai Zhong** − Qnami AG, 4132 Muttenz, Switzerland
**Florin Ciubotaru** − imec, 3001 Leuven, Belgium
**Laurentiu Stoleriu** − Department of Physics, Alexandru Ioan Cuza University, 700506 Iasi, Romania
**Alexander Stark** − Qnami AG, 4132 Muttenz, Switzerland
**Peter Rickhaus** − Qnami AG, 4132 Muttenz, Switzerland
**Felipe Fávaro de Oliveira** − Qnami AG, 4132 Muttenz, Switzerland
**Mathieu Munsch** − Qnami AG, 4132 Muttenz, Switzerland
**Paola Favia** − imec, 3001 Leuven, Belgium
**Maxim Korytov** − imec, 3001 Leuven, Belgium
**Patricia Van Marcke** − imec, 3001 Leuven, Belgium
**Patrick Maletinsky** − Qnami AG, 4132 Muttenz, Switzerland; Department of Physics, University of Basel, Basel CH-4056, Switzerland
**Christoph Adelmann** − imec, 3001 Leuven, Belgium
**Paul van der Heide** − imec, 3001 Leuven, Belgium

Complete contact information is available at:
https://pubs.acs.org/10.1021/acs.nanolett.1c03723

### Author Contributions

U.C., H.Z., F.C., and A.S. designed this work and U.C. prepared the manuscript. The experiments were carried out by U.C., H.Z., F.C., A.S., L.S., and P.F., and M.K. and P.V. have contributed to the TEM analysis. P.R., P.M., C.A., and F.F., M.M., and P.V. have contributed in the results analysis and discussion of the manuscript during all phases of the preparation. All authors reviewed the manuscript.

### Notes

The authors declare the following competing financial interest(s): F.F., H.Z., and P.M. are coinventors on a pending patent application related to a relevant method of use of scanning NV microscopy. All authors affiliated with Qnami AG declare financial interest. The remaining authors declare no competing financial interest.

## ACKNOWLEDGMENTS

## ■ REFERENCES

(1) Parkin, S. S. P.; Hayashi, M.; Thomas, L. Magnetic Domain-Wall Racetrack Memory. *Science (Washington, DC, U. S.)* **2008**, *320* (5873), 190−194.

(2) Parkin, S.; Yang, S. Memory on the Racetrack. *Nat. Nanotechnol.* **2015**, *10* (3), 195−198.

(3) Dieny, B.; Prejbeanu, I. L.; Garello, K.; Gambardella, P.; Freitas, P.; Lehndorff, R.; Raberg, W.; Ebels, U.; Demokritov, S. O.; Akerman, J.; et al. Opportunities and Challenges for Spintronics in the Microelectronics Industry. *Nat. Electron.* **2020**, *3* (8), 446−459.

(4) Talmelli, G.; Devolder, T.; Träger, N.; Förster, J.; Wintz, S.; Weigand, M.; Stoll, H.; Heyns, M.; Schütz, G.; Radu, I. P.; et al. Reconfigurable Submicrometer Spin-Wave Majority Gate with Electrical Transducers. *Sci. Adv.* **2020**, *6* (51), No. eabb4042.

(5) Wang, Q.; Kewenig, M.; Schneider, M.; Verba, R.; Kohl, F.; Heinz, B.; Geilen, M.; Mohseni, M.; Lägel, B.; Ciubotaru, F.; et al. A Magnonic Directional Coupler for Integrated Magnonic Half-Adders. *Nat. Electron.* **2020**, *3* (12), 765−774.

(6) Heinz, B.; Brächer, T.; Schneider, M.; Wang, Q.; Lägel, B.; Friedel, A. M.; Breitbach, D.; Steinert, S.; Meyer, T.; Kewenig, M.; et al. Propagation of Spin-Wave Packets in Individual Nanosized Yttrium Iron Garnet Magnonic Conduits. *Nano Lett.* **2020**, *20* (6), 4220−4227.

(7) Talmelli, G.; Narducci, D.; Vanderveken, F.; Heyns, M.; Irrera, F.; Asselberghs, I.; Radu, I. P.; Adelmann, C.; Ciubotaru, F. Electrical Spin-Wave Spectroscopy in Nanoscale Waveguides with Nonuniform Magnetization. *Appl. Phys. Lett.* **2021**, *118* (15), 152410.

(8) Sluka, V.; Schneider, T.; Gallardo, R. A.; Kákay, A.; Weigand, M.; Warnatz, T.; Mattheis, R.; Roldán-Molina, A.; Landeros, P.; Tiberkevich, V.; et al. Emission and Propagation of 1D and 2D Spin Waves with Nanoscale Wavelengths in Anisotropic Spin Textures. *Nat. Nanotechnol.* **2019**, *14* (4), 328−333.

(9) Yu, H.; d' Allivy Kelly, O.; Cros, V.; Bernard, R.; Bortolotti, P.; Anane, A.; Brandl, F.; Heimbach, F.; Grundler, D. Approaching Soft X-Ray Wavelengths in Nanomagnet-Based Microwave Technology. *Nat. Commun.* **2016**, *7* (1), 11255.

(10) Zhao, T.; Scholl, A.; Zavaliche, F.; Lee, K.; Barry, M.; Doran, A.; Cruz, M. P.; Chu, Y. H.; Ederer, C.; Spaldin, N. A.; et al. Electrical Control of Antiferromagnetic Domains in Multiferroic BiFeO3 Films at Room Temperature. *Nat. Mater.* **2006**, *5* (10), 823−829.

(11) Locatelli, A.; Bauer, E. Recent Advances in Chemical and Magnetic Imaging of Surfaces and Interfaces by XPEEM. *J. Phys.: Condens. Matter* **2008**, *20* (9), No. 093002.

(12) Rösner, B.; Finizio, S.; Koch, F.; Döring, F.; Guzenko, V. A.; Langer, M.; Kirk, E.; Watts, B.; Meyer, M.; Loroña Ornelas, J.; et al. Soft X-Ray Microscopy with 7 Nm Resolution. *Optica* **2020**, *7* (11), 1602.

(13) Hsu, P. J.; Kubetzka, A.; Finco, A.; Romming, N.; Von Bergmann, K.; Wiesendanger, R. Electric-Field-Driven Switching of Individual Magnetic Skyrmions. *Nat. Nanotechnol.* **2017**, *12* (2), 123−126.

(14) Mahmoud, A.; Ciubotaru, F.; Vanderveken, F.; Chumak, A. V.; Hamdioui, S.; Adelmann, C.; Cotofana, S. Introduction to Spin Wave Computing. *J. Appl. Phys.* **2020**, *128* (16), 161101.

(15) Rondin, L.; Tetienne, J.-P.; Hingant, T.; Roch, J.-F.; Maletinsky, P.; Jacques, V. Magnetometry with Nitrogen-Vacancy Defects in Diamond. *Rep. Prog. Phys.* **2014**, *77* (5), No. 056503.

(16) Barry, J. F.; Schloss, J. M.; Bauch, E.; Turner, M. J.; Hart, C. A.; Pham, L. M.; Walsworth, R. L. Sensitivity Optimization for NV-Diamond Magnetometry. *Rev. Mod. Phys.* **2020**, *92* (1), No. 015004.

(17) Dutta, S.; Kundu, S.; Gupta, A.; Jamieson, G.; Gomez Granados, J. F.; Bommels, J.; Wilson, C. J.; Tokei, Z.; Adelmann, C. Highly Scaled Ruthenium Interconnects. *IEEE Electron Device Lett.* **2017**, *38* (7), 949−951.

(18) Pike, C.; Fernandez, A. An Investigation of Magnetic Reversal in Submicron-Scale Co Dots Using First Order Reversal Curve Diagrams. *J. Appl. Phys.* **1999**, *85* (9), 6668−6676.

(19) Schell, A. W.; Engel, P.; Werra, J. F. M.; Wolff, C.; Busch, K.; Benson, O. Scanning Single Quantum Emitter Fluorescence Lifetime Imaging: Quantitative Analysis of the Local Density of Photonic States. *Nano Lett.* **2014**, *14* (5), 2623−2627.

(20) Donahue, M. J.; Porter, D. G. OOMMF User's Guide, Version 1.0. *NIST Publ. Interag. Rep. NISTIR* **1999**. DOI: 10.6028/NIST.IR.6376.